Available online at www.sciencedirect.com

ScienceDirect

IFAC PapersOnline CONFERENCE PAPER ARCHIVE

IFAC PapersOnLine 53-2 (2020) 12327–12333

Constrained sliding mode control for oscillating water column wave energy converters.

Daniel T. Gaebele * **Mario E. Magaña** * **Ted K.A. Brekken** *
João C.C. Henriques **

* *Oregon State University, Corvallis, OR 97331 USA (e-mail: gaebeled@oregonstate.edu, magana@eecs.oregonstate.edu , brekken@engr.orst.edu).*
** *University of Lisbon, Lisbon, Portugal (e-mail: joaochenriques@tecnico.ulisboa.pt)*

Abstract: Maintaining a setpoint to maximize energy harvest of wave energy converters (WECs) with the uncertainties induced by the ocean waves irregular excitation can be ensured by using sliding mode control. In practice, the infinite switching frequency in the sliding mode is limited by the actuators bandwidth. This work compares multiple second-order sliding mode controllers (SMC) designed for an array of floating oscillating water column (OWC) WECs with varying order of discontinuity. All algorithms enable bounding the control input to respect the physical constraints, e.g. maximal torque introduced by the generators attached to the bi-radial turbines that are driven by the oscillating motion of the air trapped inside the OWC chamber. Practical implementation of the algorithms is facilitated by a smooth approximation of the signum function and a smooth switching between different cases or hysteresis and compared to the ideal switching. The performance of the presented control laws is evaluated while maintaining a constant turbine rotational speed inside the floating OWC WEC array, and the generated power is compared to an ideal control law for different irregular sea states.

Keywords: Sliding-mode control, Renewable energy systems, Ocean wave energy, Oscillating water column

1. INTRODUCTION

Research in ocean wave energy has increased over the last decades (Falcão, 2010) and has a high potential to contribute to the energy mix of the future (Aderinto and Li, 2018). To this date, significant cost associated with the development and maintenance hamper the realization of commercially viable projects that can compete with other renewable energy sources (Andrews and Jelley, 2017). Advances can be achieved by array deployment in farms of numerous WECs (Chowdhury et al., 2015), reducing power fluctuations for grid connection and reducing cost for mooring and maintenance. The irregular nature of ocean waves makes the power optimization for a wave energy converter (WEC) an appealing task for the control design. Various WEC concepts lead to various control approaches, e.g. optimal control for linear power take-off (PTO) dynamics (Bacelli and Ringwood, 2015) and model predictive control (Richter et al., 2013). Sliding mode control (SMC), a well established approach in other fields, has been used previously due to its robustness and suitability for nonlinear uncertain dynamics in (Magaña et al., 2019) to maintain the rotational speed of the attached synchronous AC generator constant.

In this work we present higher order SMC controllers to obtain a continuous control signal while taking physical constraints, namely, maximal generator torque into account. The derivation generalizes the generator to be applicable for any kind of electric machine. Due to the faster electromagnetic dynamics, compared to the wave-body dynamics, we assume that the motor drive's torque command is ensured by the generator. The derived control laws are applied to the dynamic model of an array of devices with actual ocean deployment and testing, known as Marmok-A-5 (see (Etxaniz, 2017) for details on the buoy geometry). The Marmok-A-5 is a floating oscillating water column type (OWC).This semi-submerged hollow offshore device is open at the bottom and filled with water. Above the calm sea surface air is trapped by the power take off (PTO) turbine.OWCs have only some moving parts and since the PTO does not have water contact OWCs are considered as one of the simplest OWCs (Falcão and Henriques, 2016). As the name OWC indicates, the water inside the hollow spar oscillates up and down, inducing an alternating air flow. Therefore, self-rectifying turbines are used to capture the mechanical energy. In terms of performance the bi-radial turbine, with a peak efficiency of 79 % is a good choice compared to the well know Wells turbine (Falcão and Henriques, 2016). In this paper we use the equations of motion and the experimentally derived characteristics of the bi-radial turbine from (Henriques et al., 2017) for the implementation of the OWC array. We

⋆ This research was sponsored by the National Science Foundation (Award Number: 1711859).

10.1016/j.ifacol.2020.12.1202

present the dynamic equations for an array of N floating OWCs, which is not limited to the Marmok-A-5, but linear hydrodynamic coefficients need to be available.

The assessment of the main frequency dependent hydrodynamic coefficients is commonly conducted using the boundary element method (BEM) nowadays. With the BEM the velocity potential of the flow is solved and the results in the frequency domain are transformed into the time domain, which is required to considered nonlinearities in the dynamic model. We represent the OWC with the full column in (Gaebele et al., 2019) for the BEM simulation, instead of using a thin plate, to reduce the numerical instabilities in the results of the used BEM solver ANSYS Aqwa. The OWC is therefore represented by an rigid imaginary piston of the same dimensions.

A brief description of these analytical relationships is presented in Sec. 2. In Sec. 3 we address the control design for an array of Marmok-A-5 WECs, with the necessary concepts to implement multiple higher order sliding mode algorithms, that follow a reference speed, respect generator constraints and achieve a smooth control signal. In Sec. 4 we discuss and compare the behavior of the different control schemes based on the quality of the sliding mode and the control signal and conclude the work with a brief discussion on power improvement capabilities of the SMC.

2. DYNAMIC MODEL

The equations of motion of the array of N floating OWC WECs are described in more detail in our previous work (Gaebele et al., 2019). In this work we focus on the necessary aspects for the control design and restate the state space representation together with the assumptions the hydrodynamic model is based on.

We use linear water wave theory assuming the amplitude of the ocean waves and the body motions is small compared to the ocean wave length λ. The internal free water surface is represented by an imaginary rigid piston, since the diameter inside the buoy is $d_\mathrm{p} \ll \lambda$. This enables us to apply oscillating body theory for the floating OWC WEC. Also known as a two-body heaving system as it is called in (Falnes, 2002). Throughout this work we will use piston and OWC interchangeably. For power generation, mainly the heave axis has relevance for floating OWC WECs. Therefore, we focus on the system dynamics of the heave displacement $z(t)$, which is defined to be zero at the calm sea surface and positive for an upwards displacement. The necessary steps to include more degrees of freedom in the model and the arising cross coupling is discussed in Gaebele et al. (2019) in the appendix. For an array of N WECs, thus $2N$ bodies, let us define the state vector as

$$x = \begin{bmatrix} x_z^T & x_v^T & x_{p^*}^T & x_\Omega^T \end{bmatrix}^T. \tag{1}$$

Here x_z and x_v denote the respective vectors for heave positions and velocities of the bodies $i \dots 2N$, thus $x_{z,i} = z_i = x_i$, $x_{v,i} = \dot{z}_i = x_{2N+i}$. Furthermore, x_{p^*} represents the vector for the air chamber relative pressure differences of WEC $i \dots N$ and finally the rotational speeds of the turbine-generator sets of system $i \dots N$ are contained in the vector x_Ω , respectively, therefore $x_{p^*,i} = p_i^* = x_{4N+i}$ and $x_{\Omega,i} = \Omega_i = x_{5N+i}$.

2.1 Hydrodynamic model

After the fundamental work of (Cummins, 1962) the oscillation of body floating in the ocean can be described by,

$$m_i \ddot{x}_{z,i}(t) = F_i^\mathrm{H}(t) + F_i^\mathrm{M}(t) + F_i^\mathrm{Ex}(t) + F_i^\mathrm{R}(t) + F_i^\mathrm{PTO}(t). \tag{2}$$

Here m_i represents the physical mass of the i^{th} body. The forces considered in (2) are,

- $F^\mathbf{H}$**:** The hydrostatic restoring force, adding heave position depending spring like effect, zero at equilibrium $x_{z,i}(t) = 0$.
- $F^\mathbf{M}$**:** The mooring force due to mooring connection with the sea floor. No mooring is connected to the imaginary piston.
- $F^\mathbf{Ex}$**:** The wave induced excitation force, which accounts for all incident waves on the body. Results from solving the diffraction problem of the incident wave field inside the array. F^Ex is obtained by superposing 100 wave components that are randomly phase shifted, using a Pieson-Moskowitz wave energy spectrum. Different array configurations are taken into account with the hydrodynamic excitation force coefficient and the corresponding phase coefficient for the respective WECs and geometries.
- $F^\mathbf{R}$**:** The radiation force, including interactions with the motion of other bodies in the array. It results from solving the radiation problem and is composed out of:
  - $F_i^{\mathbf{R},\infty}$ explicitly depending on the acceleration $\ddot{x}_{z,j}$ multiplied with the constant linear hydrodynamic coefficient A_{ij}^∞, known as the added mass evaluated at $\omega \to \infty$.
  - $F_i^\mathbf{R'}$ explicitly depending on the velocity $\dot{x}_{z,j}$ of the j^{th} body and the inverse Fourier transformation of the frequency dependent radiation damping coefficient $B_{ij}(\omega)$. This force takes the bodies past motion into account and instead of a time convolution we approximate $F_i^\mathrm{R'}$ with a linear state space system with the same step response.
- $F^\mathbf{PTO}$**:** The force due to the pressure change in the chamber induced by the turbine-generator dynamics. It is acting in opposite direction for buoy and OWC.

Nonlinear viscous and other friction effects are neglected in this work, because of the ring torus shaped of the buoys bottom reducing viscous losses. Nevertheless, time-domain formulation necessary for the nonlinear PTO dynamics keeps the option to include those practical correction terms (Falnes, 2002).

The buoy and piston move relative to each other changing the volume at pressure $p_{\mathrm{c}_i}(t)$ of the air chamber. The difference to the constant atmospheric pressure $p_{\mathrm{c}_i}(t) - p_\mathrm{at}$ results in a force when multiplied with the piston surface S_p, namely,

$$F_i^\mathrm{PTO}(t) = \begin{cases} \big(p_{\mathrm{c}_i}(t) - p_\mathrm{at}\big) S_\mathrm{p}, & \text{for a buoy} \\ -\big(p_{\mathrm{c}_i}(t) - p_\mathrm{at}\big) S_\mathrm{p}, & \text{for a piston} \end{cases}, \tag{3}$$

acting in opposite direction for the two bodies in the heaving system. Apart from the heave motion, the turbine air flow and consequently the PTO dynamics with influence the rate of change of the chamber pressure.

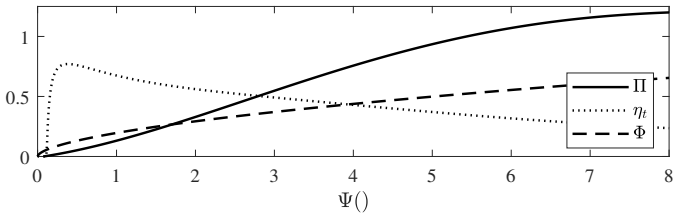

Fig. 1. Dimensionless turbine characteristics as functions of the dimensionless pressure head Ψ. Namely, efficiency η, flow rate Φ and power coefficient Π from (Henriques et al., 2017)

2.2 Power Take-Off model

In (Henriques et al., 2017) detailed nonlinear modeling and experiments of the air chamber in OWCs together with the biradial turbine is available. A suitable generator for this type of turbine is investigated in (Henriques et al., 2019). We recapitulate the main equations necessary to derive a relation for the pressure rate of change inside the chamber and consequently the turbine torque. First we define the state variable, the dimensionless relative chamber pressure,

$$x_{p^*,i}(t) = p_i^*(t) = \frac{p_{\mathrm{c}_i}(t)}{p_{\mathrm{at}}} - 1, \tag{4}$$

with the atmospheric pressure p_{at} and the corresponding density is denoted ρ_{at}. The derivation is based on a mass balance of the chamber with the air density ρ_{c_i} and the instantaneous chamber volume $V_{\mathrm{c}_i}(t)$ is determined by the relative position of piston and buoy. Assuming that air acts as a perfect gas for expansion yields

$$\rho_{\mathrm{c}_i}(t) = \rho_{\mathrm{at}}(x_{p^*,i}(t)+1)^{\frac{1}{\gamma}}, \tag{5}$$

with the specific heat ratio $\gamma \approx 1.4$. We take the logarithmic derivative $L(f) := \dot{f}/f$ of (5) and substitute into the mass balance which results in

$$\dot{x}_{p^*,i}(t) = -\gamma \frac{\dot{m}_{\mathrm{t}_i}(t)}{\rho_{\mathrm{at}} V_{\mathrm{c}_i}(t)} \Big(x_{p^*,i}(t)+1\Big)^{\frac{\gamma-1}{\gamma}} - \gamma \frac{\dot{V}_{\mathrm{c}_i}(t)}{V_{\mathrm{c}_i}(t)} \Big(x_{p^*,i}(t)+1\Big). \tag{6}$$

Here the mass flow through the turbine $\dot{m}_{\mathrm{t}_i}(t)$ is determined with the turbine dynamics. In this work we model the time rate change of the angular turbine/generator velocity with

$$\dot{x}_{\Omega,i}(t) = \dot{\Omega}_i = \frac{1}{J_{\mathrm{t}}}\big(T_{\mathrm{turb}_i} - T_{\mathrm{gen}_i} - B_{\mathrm{t}} x_{\Omega,i}\big), \tag{7}$$

where J_{t} is the composite moment of inertia (MOI) of the i^{th} turbine / generator set. The instantaneous torques T_{turb_i} and T_{gen_i} are determined by the i^{th} turbine and the generator, respectively. Vicious friction of the turbine/generator is modeled linear using the constant B_{t}. The generator torque is defined to be the control input

$$u_{\mathrm{gen},i} = T_{\mathrm{gen},i}, \tag{8}$$

to our system. The turbine torque is identified with the pressure dependent dimensionless performance characteristics illustrated in Fig. 1. To normalize those values, the rotational speed $x_{\Omega,i}$, the turbine diameter d_{t} and the reference air density $\rho_{\mathrm{in},i}$ are used. Depending on an inhalation, or exhalation $\rho_{\mathrm{in}_i} = \max\big(\rho_{\mathrm{at}}, \rho_{\mathrm{c}_i}(t)\big)$.

The dimensionless pressure head can now be computed as

$$\Psi_i(x_{p^*,i}, x_{\Omega,i}) = \frac{p_{\mathrm{at}} x_{p^*,i}}{\rho_{\mathrm{in}_i} x_{\Omega,i}^2 d_{\mathrm{t}}^2}. \tag{9}$$

Now $\dot{m}_{\mathrm{t}_i}$ can be obtained as a function of $\Phi_i(\Psi_i)$ with the experimental results from Fig. 1. The turbine torque is computed out of the introduced characteristics and variables, namely

$$T_{\mathrm{t}_i} = \rho_{\mathrm{in}_i} x_{\Omega,i}^2 d_{\mathrm{t}}^5 \Pi_i(\Psi_i). \tag{10}$$

2.3 State Space Representation

The state space representation of the physical dynamical equations of the WEC system is given by

$$\dot{\boldsymbol{x}} = \begin{bmatrix} \dot{\boldsymbol{x}}_z \\ \dot{\boldsymbol{x}}_v \\ \dot{\boldsymbol{x}}_{p^*} \\ \dot{\boldsymbol{x}}_\Omega \end{bmatrix} = \begin{bmatrix} \boldsymbol{x}_v \\ (\boldsymbol{M})^{-1} \cdot \boldsymbol{\mathcal{F}}(\boldsymbol{x}) \\ f_{\mathrm{p}}(\boldsymbol{x}) \\ f_{\mathrm{k}}(\boldsymbol{x}_{p^*}, \boldsymbol{x}_\Omega, \boldsymbol{u}_{\mathrm{gen}}) \end{bmatrix} \tag{11}$$

with

$$\boldsymbol{M} = \begin{bmatrix} A_{11}^\infty & \dots & A_{1N}^\infty & \dots & A_{12N}^\infty \\ \vdots & \ddots & \vdots & \ddots & \vdots \\ A_{N1}^\infty & \dots & A_{NN}^\infty & \dots & A_{N2N}^\infty \\ \vdots & \ddots & \vdots & \ddots & \vdots \\ A_{2N1}^\infty & \dots & A_{2NN}^\infty & \dots & A_{2N2N}^\infty \end{bmatrix} + \mathrm{diag}\left(\begin{bmatrix} m_1 \\ \vdots \\ m_N \\ \vdots \\ m_{2N} \end{bmatrix} \right). \tag{12}$$

Here $(\boldsymbol{M})^{-1}$ represents the interaction between all bodies due to the multiplication with the composite force $\boldsymbol{\mathcal{F}}(\boldsymbol{x})$. It originates while isolating the highest derivatives on the left hand sight of the equations of motion from the radiation force component $F_i^{\mathrm{R},\infty}$. The matrix $\boldsymbol{M}$ consist of the constant added mass components A_{ii}^∞ and the sum with the bodies physical masses m_i on its diagonal. The composite force sums up all forces that would act on a single body, namely,

$$\boldsymbol{\mathcal{F}}(\boldsymbol{x}) = \begin{bmatrix} F_1^{\mathrm{H}}(x_1) + F_1^{\mathrm{M}}(x_1) + F_1^{\mathrm{PTO}}(p_1^*) + F_1^{\mathrm{R'}}(\boldsymbol{x}_v) + F_1^{\mathrm{Ex}} \\ \vdots \\ F_{2N}^{\mathrm{H}}(\cdot) + F_{2N}^{\mathrm{M}}(\cdot) + F_{2N}^{\mathrm{PTO}}(\cdot) + F_{2N}^{\mathrm{R'}}(\cdot) + F_{2N}^{\mathrm{Ex}} \end{bmatrix}. \tag{13}$$

3. CONTROL DESIGN

Our control algorithm aims to have the WEC turbine follow a reference angular velocity Ω_{ref} while respecting the physical constraints of the generator by applying a smooth control signal to avoid stress on the actuators. To achieve these goals we apply different sliding mode controllers (SMCs) that force the WEC system to reach and stay in a subset of the state space known as the sliding surface, i.e. $\sigma(t,x) = 0$. We define the sliding variable as the error between Ω_{ref} and the instantaneous rotational speed, namely,

$$\sigma(t,x) = \Omega_{\mathrm{ref}} - x_\Omega = 0. \tag{14}$$

The control algorithms are applied to each of the three devices taking into account the WEC array hydrodynamic interaction using the numerical values of the physical bounds, which are computed in the ensuing section. In what follows, we omit the subscript $_i$ when deriving the control algorithms.

The control effort is based on the position of the state relative to $\sigma(t,x) = 0$ and generally speaking the SMC steers the state trajectory towards it and brings it back to it if it leaves it. Theoretically, this would happen at infinite

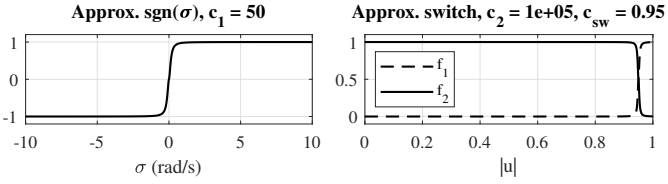

Fig. 2. Approximation of the signum function (left) and the smooth approximation of the switch (right)

frequency resulting in a discontinuous control signal it. In practice, imperfections like delays prevent the infinite frequency switching and consequently the ideal sliding. The result is an oscillation of the states around the sliding surface which yields a chattering in the control signal. This can be damaging for the actuators, thus our second goal is to achieve a trade off between staying in a neighborhood of $\sigma(t,x)=0$ and achieving a smooth control signal.

We use an ideal feedback control law developed in (Henriques et al., 2017, 2019) to help us estimate the expected range of state values and to compare the SMC to, namely,

$$u_{\text{gen}} = \min\left(a_{\text{gen}} x_{\Omega}^{b_{\text{gen}}-1},\, P_{\text{gen}}^{\text{rated}}/x_{\Omega},\, T_{\text{gen}}^{\max}\right). \tag{15}$$

The authors developed this control law for a practical implementation, based on the maximization of the aerodynamic efficiency of a fixed OWC, equipped with the same biradial turbine. In this work we set the coefficients to $a_{\text{gen}} = 0.0001$ and $b_{\text{gen}} = 3.6$ following (Henriques et al., 2017) for the same order of magnitude and we cannot guarantee optimal values for the simulated sea state. However, they are suitable for initial evaluation system behaviour for a WEC array.

In subsection 3.1 we address how we can practically implement higher order SMC algorithms by using two smooth approximations of discontinuous functions. In subsection 3.2 we state the system requirements that are necessary to apply the integral SMC following the methodology presented in (Levant, 1993) and we obtain the positive constants bounding various derivatives of $\sigma(t,x)$ either analytically, or numerically with the help of the derived simulation model and (15). In subsection 3.3 we present four different SMC algorithms from (Levant, 1993) that can be applied to the OWC WEC array followed by brief conceptual description of convergence guarantee.

3.1 Practical implementation

Most SMC algorithms use the `sgn` (signum) function to evaluate on which side of the sliding surface the state trajectory is. To influence this discontinuous hard transition either between -1 and 1 or between the cases used in the SMC algorithms we adapt the function

$$h(y,c) = \frac{y\,(1+c|y|)}{1+|y|\,(1+c|y|)}, \quad c\in\mathbb{R}^{+}, \tag{16}$$

used in (Magaña et al., 2019) where y is the variable determining the switch and c controls the sharpness of the switch. All `sgn` functions in the following control schemes are approximated with

$$\operatorname{sgn}(\sigma(t)) \cong h(\sigma(t), c_1) \tag{17}$$

as illustrated in Fig. 2 to decrease the chattering when the state trajectory crosses σ. The algorithms in Sec. 3.3 all switch the time rate of change $\dot{u}$ as soon as the control signal exceeds the predefined limit c_{sw}, thus counteracting the control effort. We normalise $|u| \in (0,1)$, such that for $|u| = 1$ the generator applies the maximal torque. With $c_{\text{sw}} < 1$ we can further influence to what percentage the physical constraint should be exploited and we use $c_{\text{sw}} = 0.95$ in what follows. In other words,

$$\dot{y} = \begin{cases} f_1, & \text{if } |y| > c_{\text{sw}} \\ f_2, & \text{if } |y| \le c_{\text{sw}} \end{cases} \tag{18}$$

$$\cong \frac{1}{2}\Big(f_1\big(h(y_{\text{sw}}, c_2)+1\big) + f_2\big(-h(y_{\text{sw}}, c_2)+1\big)\Big), \tag{19}$$

with $y_{\text{sw}} = y - c_{\text{sw}}$. The transition is illustrated in the right plot in Fig. 2. A second idea to diminish the chattering when the torque limit is reached is to introduce a hysteresis to smooth out the back and forth between functions f_1 and f_2. We implement the behavior with the Simulink `relay` block with a switch on at $|u| = 1$ and switch off at $|u| = 0.95$. However, this still introduces a hard transition as illustrated in the next section.

3.2 System requirements

In this subsection we show that the model of the WEC array meets the system requirements to apply the SMC methodologies from the work of (Levant, 1993) and how we can obtain numerical values for the positive constants K_{m}, K_{M} and C_0. Equation (11) can be rewritten as

$$\dot{x} = f(x(t), u_{\text{gen}}), \tag{20}$$

where f satisfies class C^1. Again, here $u_{\text{gen}} = T_{\text{gen}}$ is physically constrained to a maximal constant value $T_{\text{gen}}^{\max}$, thus we introduce the dimensionless control input $u = \frac{1}{T_{\text{gen}}^{\max}} u_{\text{gen}}$ with $|u| \le c_{\text{sw}}$. The sliding variable $\sigma(t,x)$ is of class C^2. The differential operator considering u constant

$$\mathcal{L}_u = \frac{\partial}{\partial t}(\cdot) + \frac{\partial}{\partial x}(\cdot) f(x, u_{\text{gen}}) \tag{21}$$

represents the total derivative with respect to (20). Define

$$\dot{\sigma}(t,x,u) = \mathcal{L}_u \sigma(t,x). \tag{22}$$

Now assume there exists a set $C = \{(t,x,u)\} : |\sigma(t,x)| < \sigma_0$, where σ_0 is called the linearity region, such that

$$0 < K_{\text{m}} < \left|\frac{\partial \dot{\sigma}}{\partial u}\right| < K_{\text{M}}. \tag{23}$$

With the positive constants $K_{\text{m}}, K_{\text{M}}$. Moreover, we require the boundedness of the second derivative of the sliding surface, namely,

$$|\mathcal{L}_u \mathcal{L}_u \sigma(t,x)| < C_0. \tag{24}$$

Let us obtain the bounds in (23)

$$\dot{\sigma}(t,x,u_{\text{gen}}) = \mathcal{L}_u \sigma(t,x) \tag{25}$$

$$= 0 + [0\ \cdots\ -1]\, \boldsymbol{f}(x, u_{\text{gen}}) \tag{26}$$

$$= -f_{\text{k}}(x_{p^*}, x_{\Omega}, u_{\text{gen}}) \tag{27}$$

$$= -J_{\text{t}}^{-1}\big(T_{\text{turb}}(x_{p^*}, x_{\Omega}) - u_{\text{gen}} - B_{\text{t}} x_{\Omega}\big), \tag{28}$$

with $u_{\text{gen}} = T_{\text{gen}}^{\max} u$ it directly follows

$$\frac{\partial \dot{\sigma}}{\partial u} = \frac{T_{\text{gen}}^{\max}}{J_{\text{t}}}. \tag{29}$$

We choose

$$K_{\text{m}} = \frac{3}{4}\frac{|T_{\text{gen}}^{\max}|}{J_{\text{t}}} \quad K_{\text{M}} = \frac{5}{4}\frac{|T_{\text{gen}}^{\max}|}{J_{\text{t}}}. \tag{30}$$

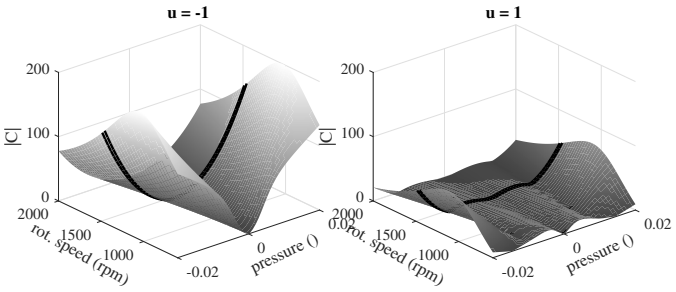

Fig. 3. The second derivative of the sliding surface with the minimal (left) and maximal (right) value for the generator torque.

Now, consider a fixed pressure and rotational speed x_{p^*}, x_Ω = constant, thus Ψ = constant and therefore Φ, η = constant, consequently T_{turb} = constant with respect to time. Now,

$$\ddot{\sigma} = \mathcal{L}_u \mathcal{L}_u \sigma(t,x) \tag{31}$$

$$= {J_\text{t}}^{-1} \left(B_\text{t} \dot{x}_\Omega - 2T_\text{turb}(x_{p^*}, x_\Omega)/x_\Omega + T_\text{gen}^\text{max} \dot{u} \right) \tag{32}$$

$$= \underbrace{{J_\text{t}}^{-2} \left(B_\text{t} - 2/x_\Omega \right) \left(T_\text{turb} - T_\text{gen}^\text{max} u + B_\text{t} x_\Omega \right)}_{C(x_{p^*}, x_\Omega, u)} + \underbrace{T_\text{gen}^\text{max}/J_\text{t}}_{K} \dot{u}. \tag{33}$$

We can now obtain an upper bound C_0 by numerically computing $|C(x_{p^*}, x_\Omega, u)|$ for the minimal and maximal values of the control and varying x_Ω and x_{p^*}, illustrated in Fig. 3 with the linearity region σ_0 being inside the dashed lines on the surface.

3.3 Algorithms

All four control algorithms achieve the main goals of following Ω_ref and respecting the generator torque limit, though the control signals are not equally smooth. The algorithms are given in their original form with the discontinuous `sgn` functions and cases as in (Levant, 1993), but are simulated with the approximations described earlier. First, we introduce the A_μ - algorithm

$$\dot{u} = \begin{cases} -u, & \text{if } |u| > c_\text{sw} \\ -\alpha_1 \operatorname{sgn}\sigma, & \text{if } |u| \leq c_\text{sw}, \end{cases} \tag{34}$$

which is a first order real sliding algorithm, with $\alpha_1 > 0$. Second we have the twisting algorithm (TW)

$$\dot{u} = \begin{cases} -u, & \text{if } |u| > c_\text{sw} \\ -\alpha_\text{m} \operatorname{sgn}\sigma, & \text{if } \sigma\dot{\sigma} \leq 0,\ |u| \leq c_\text{sw} \\ -\alpha_\text{M} \operatorname{sgn}\sigma, & \text{if } \sigma\dot{\sigma} > 0,\ |u| \leq c_\text{sw} \end{cases} \tag{35}$$

where $\alpha_\text{M} > \alpha_\text{m} > 0$ and chosen such that

$$\alpha_\text{m} > \max\left(\frac{4K_\text{M}}{\sigma_0}, \frac{C_0}{K_\text{m}} \right) \tag{36}$$

$$\alpha_\text{M} > \frac{K_\text{M}}{K_\text{m}} \alpha_\text{m} + C_0 \left(1 + \frac{1}{K_\text{m}} \right). \tag{37}$$

The next algorithm drives σ and $\dot{\sigma}$ towards 0 and is therefore named super-twisting algorithm (STW).

$$\dot{u} = \begin{cases} -u, & \text{if } |u| > c_\text{sw} \\ -\alpha_2 \operatorname{sgn}(\dot{\sigma} - g(\sigma)), & \text{if } |u| \leq c_\text{sw} \end{cases} \tag{38}$$

with

$$g(\sigma) = -\lambda_2 \operatorname{sgn}\sigma |\sigma|^\gamma, \tag{39}$$

and $\lambda_2 > 0$ and $0.5 \leq \gamma < 1$. An algorithm similar to the twisting algorithm but independent of $\dot{\sigma}$ (TW-$\dot{\sigma}$), namely,

$$u = u_1 + u_2 \tag{40}$$

$$\dot{u}_1 = \begin{cases} -u, & \text{if } |u| > c_\text{sw} \\ -\alpha_3 \operatorname{sgn}\sigma, & \text{if } |u| \leq c_\text{sw} \end{cases} \tag{41}$$

$$u_2 = \begin{cases} -\lambda_3 |\sigma_0|^\rho \operatorname{sgn}\sigma, & \text{if } |\sigma| > \sigma_0 \\ -\lambda_3 |\sigma|^\rho \operatorname{sgn}\sigma, & \text{if } |\sigma| \leq \sigma_0 \end{cases} \tag{42}$$

Here the design parameters have to satisfy the inequalities

$$\alpha_3 > \max\left(\frac{4K_\text{M}}{\sigma_0}, \frac{C_0}{K_\text{m}} \right) \tag{43}$$

$$\rho \left(\lambda_3 K_\text{m} \right)^{\frac{1}{\rho}} > \left(K_\text{M} \alpha_3 + C_0 \right) \left(2K_\text{M} \right)^{\frac{1}{\rho} - 2}, \tag{44}$$

where $\rho \in (0,1)$ and $\lambda_3 > 0$.

3.4 Convergence

The proof of stability for the algorithms herein used is presented in (Levant, 1993). The control laws all steer the rotational speed trajectory into the linear region $|\sigma(x)| < \sigma_0$. With the respective bounds it is guaranteed that control laws are capable of keeping the system dynamics in a neighborhood of the sliding surface as seen in the left column of Fig. 7. The algorithms produce switching surface trajectories which converge to a neighborhood of the origin of the σ-$\dot{\sigma}$ plane depending on their functions when $|u| \leq c_\text{sw}$. In case the control limit is reached, the dynamics may leave the sliding surface, however, the oscillating nature of ocean waves always enables the algorithms to re-reach the sliding surface.

4. NUMERICAL SIMULATIONS AND DISCUSSION

We present the simulation results of six different control cases, namely, A_μ- algorithm, twisting (TW) and super twisting (STW) algorithm and a twisting algorithm independent of $\dot{\sigma}$ (TW-$\dot{\sigma}$). Furthermore, we take a look at two additional cases of the STW, namely, a non-approximated hard and "ideal" switch (STW-i) and a switch realized with a hysteresis (STW-h). The numerical simulations are conducted with MATLAB-Simulink using stiff, variable time step solvers, except for (STW-i) when a fixed time step solver is necessary, due to infinite chattering frequency and the solver trying to decrease the step size more and more, not allowing fast simulation. Simulating the computer model faster than the actual time was our requirement when choosing the solvers for the other algorithms. Therefore, A_μ, TW and TW-$\dot{\sigma}$ algorithms require `ode15s` instead of the slower `ode23s` used for the STW algorithms, which showed less chattering, thus less computational effort. In table 1 we show an overview of the solvers, together with the figures showing the simulation results of the respective algorithm. To test the algorithms we use an

Algorithm	A_μ	TW	STW-i	STW	STW-h	TW-$\dot{\sigma}$
`ode` solver	`15s`	`15s`	`4`	`23s`	`23s`	`15s`
Δt	var.	var.	1e-4	var.	var.	var.
Fig. 7 row	1	2	3	4	5	6
x_Ω, T Fig.	6	6	5	5	6	6

Table 1. Algorithm overview.

interacting array of $N = 3$ Marmok-A-5 devices, but the

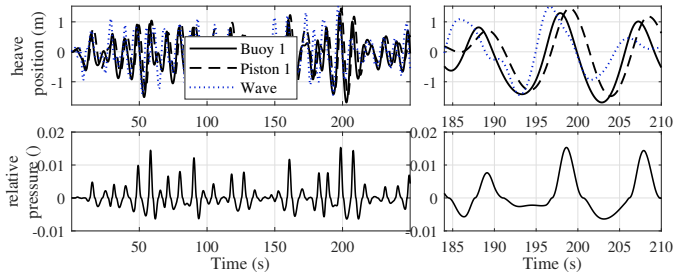

Fig. 4. Heave positions of WEC 1 bodies with the wave elevation and dimensionless relative pressure x_{p^*}.

presented results are from WEC 1 to avoid overcrowding the plots. All numerical simulation parameters are listed in table 2. We use the parameters of a SIEMENS IEC low-voltage electrical generator, model 1LE1603-2AB53-4GB4-Z, as it was connected to the bi-radial turbine in (Henriques et al., 2019) and set the reference rotational speed to the generator nominal speed $\Omega_{\text{ref}} = \Omega_{\text{gen}}^{\text{nom}}$. For a synchronous generator we would set Ω_{ref} to the synchronous speed. The time evolution of the position of buoy,

Quantity	sym/var	value
diameter turbine	d_{t}	0.5 m
MOI turbine+generator	J_{t}	5.24 kg m^2
friction turbine+generator	B_{t}	0.03 N m s
reference / nominal gen. speed	$\Omega_{\text{ref}}, \Omega_{\text{gen}}^{\text{nom}}$	1470 rpm
maximal generator torque	$T_{\text{gen}}^{\text{max}}$	216.5 N m
rated generator power	$P_{\text{gen}}^{\text{rated}}$	30 kW
max. generator rot. speed	$\Omega_{\text{gen}}^{\text{max}}$	3000 rpm
sea states characteristics	θ, T_{s}, H_{s}	15°, 11 s, 2.5 m
Lower / Upper bound $\frac{\partial \dot{\sigma}}{\partial u}$	K_{m}, K_{M}	30.9, 51.7
Upper bound $\ddot{\sigma}$	C_0	150
linearity region	σ_0	1 rad s^{-1}
switching smoothness	$c_1; c_2$	50 ; 100e3
switch limit	c_{sw}	0.95
A_μ - algorithm constant	α_1	10
Twisting algorithm (TW)	$\alpha_{\text{m}}, \alpha_{\text{M}}$	206.6, 500
Super twisting alg. (STW)	α_2, λ_2, γ	4.8, 9.7, 0.5
Twisting indep. of $\dot{\sigma}$ (TW-$\dot{\sigma}$)	α_3, ρ, λ_3	4.8, 0.1, 0.33

Table 2. Numerical simulation parameters.

piston and wave elevation, characterized by a significant wave height of $H_{\text{s}} = 2.5\,\text{m}$, an energy period $T_{\text{s}} = 11\,\text{s}$ and an incident wave angle $\theta = 15°$, together with the resulting dimensionless pressure difference is illustrated in Fig. 4. A close up of the time interval from 184s to 210s is illustrated, because we observe the highest x_{p^*}, since the oscillation of buoy and piston are out of phase. In this time interval the limit for the control torque will be reached two times and is suitable to illustrate the trajectory of the control signal on the sliding surfaces in Fig. 7. The maximum value of $x_{p^*} = 0.0165$ is smaller than 0.02, which is assumed for the bound C_0. In Fig. 5 we present the full time evolution of the control torque T_{gen} and the resulting rotational speed x_Ω for the two algorithms with the smoothest control signal, namely the STW controls laws with the ideal hard switching (dashed, STW-i) and the smooth implementation (solid, STW) of the same control law plus a comparison with the aerodynamically ideal feedback control law (15). When the control torque limit is reached at $t = 198\,\text{s}$ the rotational speed leaves the linear region σ_0. The extreme close up

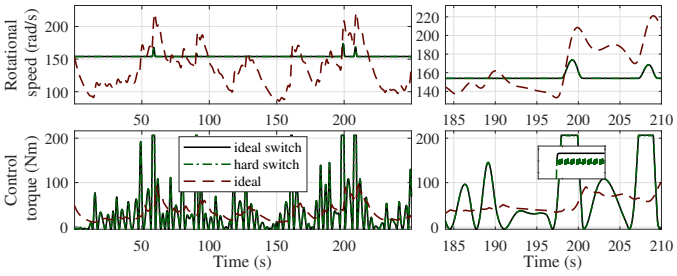

Fig. 5. Rotational speed and control torque of the STW algorithms with the hard switch and smopth switch.

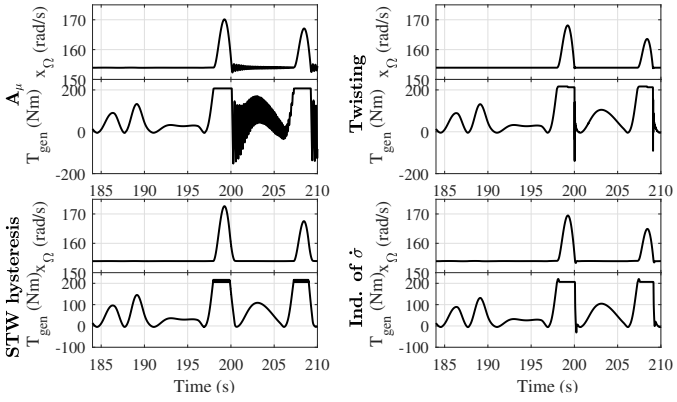

Fig. 6. Rotational speed and control torque for the different algorithms. Top left: A_μ, top right: TW, bottom left: STW-h, bottom right TW-$\dot{\sigma}$.

shows that STW-i does indeed chatters at the control limit. In Fig. 6 we illustrate Ω and T_{gen} in the close up time interval for the remaining algorithms. The A_μ algorithm shows a strong chattering after the limit is reached, also observable in Fig. 7 when the control effort u oscillates in the u-σ plane. If a non-stiff solver is used the control signal will always chatter. The twisting algorithm shows the same overshoot after the limit is reached, however, the chattering is damped in milliseconds. Nevertheless, the behavior going from maximal torque to motor mode is not desirable. The super twisting algorithm with hysteresis (STW-h) does not overshoot, but chatters while running at torque limit. In Fig. 7 the behaviour can be observed while the trajectory loops in the $\dot{\sigma}$-σ plane for $u \in [0.95; 1]$. The algorithm independent of $\dot{\sigma}$ (TW-$\dot{\sigma}$) seems to have a small overshoot before the operation at the torque limit is reached. Nevertheless, the (TW-$\dot{\sigma}$) does switch into motor mode after leaving the limit operation, since u undershoots without the knowledge of the change rate $\dot{\sigma}$. The two time intervals when control limit is reached in Fig. 5 and 6 yield the two loops of different radius in the right plot in Fig. 7 when the linear region is left. Illustrating those torque limits made us choose this sea state. Generally with the SMC compared to (15) the decrease in the variations of the rotational speed results in an increase in the variations of the generated power. Averaging the generated power over 500 s simulation time, (excluding the first 20 s to reach steady state behavior) does not yield an increase in mechanical energy production for this specific sea state with the STW controller. However, when the generator efficiency is considered an improvement of electrical energy of 7% is achieved since the constant rotation enables the

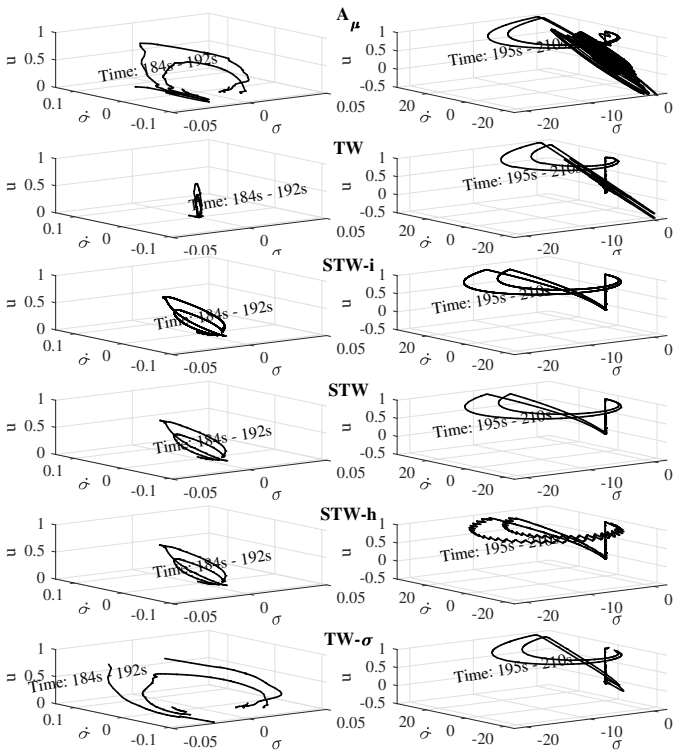

Fig. 7. Trajectory of the control signal u versus $\dot{\sigma}$ and versus σ for the different SMC algorithms. Left column in the linear region σ_0, right column when the control limit is reached.

generator to operate in a highly efficient area. The power quotient matrix in Fig. 8 illustrates that in less energetic sea states, but $H_s \geq 1$ the SMC yields on average 6-13% more mechanical energy and 35-49% more electrical energy.

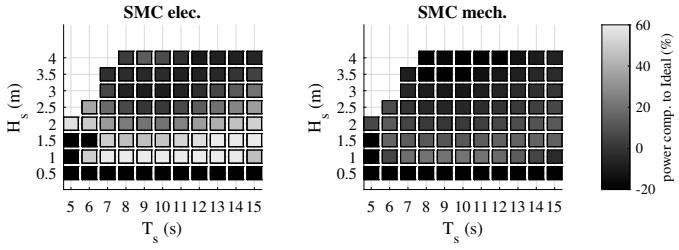

Fig. 8. Quotient between the generated power of the super twisting algorithm and the ideal control law. Left: electrical power. Right: electromechnical power.

REFERENCES

Aderinto, T. and Li, H. (2018). Ocean wave energy converters: Status and challenges. *Energies*, 11, 1250. doi:10.3390/en11051250.

Andrews, J. and Jelley, N. (2017). *Energy Science - Principles, Technologies, and Impacts, 3rd ed.* Oxford University Press.

Bacelli, G. and Ringwood, J.V. (2015). Numerical optimal control of wave energy converters. *IEEE Transactions on Sustainable Energy*, 6(2), 294–302. doi: 10.1109/TSTE.2014.2371536.

Chowdhury, S., Nader, J.R., Madrigal Sanchez, A., Fleming, A., Winship, B., Illesinghe, S., Toffoli, A., Babanin, A., Penesis, I., and Manasseh, R. (2015). A review of hydrodynamic investigations into arrays of ocean wave energy converters. *arXiv preprint*.

Cummins, W. (1962). The impulse response function and ship motions. *Symposium on Ship Theory at the Institut für Schiffbau der Universität Hamburg*.

Etxaniz, P. (2017). Wave energy: An industry with a bright future. In *Bilbao Marine Energy Week*.

Falcão, A.F. de O. (2010). Wave energy utilization: A review of the technologies. *Renewable and Sustainable Energy Reviews*, 14(3), 899 – 918. doi: 10.1016/j.rser.2009.11.003.

Falcão, A.F. de O. and Henriques, J.C.C. (2016). Oscillating-water-column wave energy converters and air turbines: A review. *Renewable Energy*, 85, 1391 – 1424. doi:10.1016/j.renene.2015.07.086.

Falnes, J. (2002). *Ocean Waves and Oscillating Systems*. Cambridge University Press.

Gaebele, D.T., Magaña, M.E., Brekken, T.K.A., and Sawodny, O. (2019). State space model of an array of oscillating water column wave energy converters with inter-body hydrodynamic coupling. *Ocean Engineering*. doi:10.1016/j.oceaneng.2019.106668.

Henriques, J.C.C., Portillo, J.C.C., Sheng, W., Gato, L.M.C., and Falcão, A.F. de O. (2019). Dynamics and control of air turbines in oscillating-water-column wave energy converters : Analyses and case study. *Renewable and Sustainable Energy Reviews*, 112(June), 571–589. doi:10.1016/j.rser.2019.05.010.

Henriques, J.C.C., Sheng, W., Falcão, A.F. de O., and Gato, L.M.C. (2017). A comparison of biradial and Wells air turbines on the Mutriku breakwater OWC wave power plant. In *ASME 2017 36th International Conference on Ocean, Offshore and Arctic Engineering*. doi:10.1115/OMAE2017-62651.

Levant, A. (1993). Sliding order and sliding accuracy in sliding mode control. *International Journal of Control*, 58(6), 1247–1263. doi:10.1080/00207179308923053.

Magaña, M.E., Brown, D.R., Gaebele, D.T., Henriques, J.C.C., and Brekken, T.K.A. (2019). Sliding Mode Control of an Array of Three Oscillating Water Column Wave Energy Converters to Optimize Electrical Power Generation. In *European Wave and Tidal Energy Conference Series*, 1–10.

Richter, M., Magaña, M.E., Sawodny, O., and Brekken, T.K.A. (2013). Nonlinear Model Predictive Control of a Point Absorber Wave Energy Converter. *IEEE Transactions on Sustainable Energy*, 4(1), 118–126. doi: 10.1109/TSTE.2012.2202929.